International Journal of Heat and Mass Transfer 254 (2026) 127590

Contents lists available at ScienceDirect

International Journal of Heat and Mass Transfer

journal homepage: www.elsevier.com/locate/ijhmt

Experimental investigation of LN_2 pool boiling critical heat flux (CHF) and development of new correlation for all cryogens, accounting for effects of surface material and size, pressure, subcooling, and surface orientation

Dylan Foster [a], Steven Darges [a], Nishad Damle [a], Sunjae Kim [a], Issam Mudawar [a,*], Jason Hartwig [b]

[a] Purdue University Boiling and Two-Phase Flow Laboratory (PU-BTPFL), School of Mechanical Engineering, Purdue University, 585 Purdue Mall, West Lafayette, IN 47907, USA
[b] Fluids and Cryogenics Branch, NASA Glenn Research Center, 21000 Brookpark Rd, Cleveland, OH 44135, USA

ARTICLE INFO

Keywords:
Cryogenics
Pool boiling
Critical heat flux, Size effects, Material effects

ABSTRACT

As the aerospace community prepares to establish humanity's permanence on the Moon and Mars, Cryogenic Fluid Management (CFM) technologies have proven themselves paramount to the established architecture of interplanetary travel. It will therefore be necessary to understand the two-phase physics inherent to cryogenic fluids. This study includes experimental investigation into saturated pool boiling critical heat flux (CHF) for liquid nitrogen (LN_2). The obtained data aid in understanding effects of two important parameters which are underrepresented in the historical database: heated surface thermophysical properties and heated surface size. With a diameter of over 100 mm, the heated surfaces tested in this study are significantly larger than those adopted in prior studies and representative of 'infinitely' large surfaces for which theoretical CHF models have been constructed. This study also includes data for three surface materials: copper, aluminum, and stainless steel, and pressures ranging from 101 to 448 kPa. By comparing the present data with those from the historical database, it is shown that CHF increases with increases in both surface size and thermal conductivity but reaches an asymptotic level for large surfaces that is independent of both parameters. Using both the current LN_2 and those of all cryogens from the historical database, a new correlation is developed which shows a MAE of 18.03% against 1181 datapoints across different cryogens, different heated surface materials and sizes, pressures, subcoolings, and surface orientations.

1. Introduction

1.1. Terrestrial and microgravity cryogenic fluid management

Due to their unique properties, cryogenic fluids have garnered significant interest across a wide range of applications. These fluids are characterized by extremely low saturation temperatures compared to conventional working fluids. Moreover, their thermophysical properties, such as exceptionally low latent heat of vaporization and surface tension, give rise to distinctive boiling behaviors. For decades, cryogens have been successfully employed in various industries. Beyond Earth's gravitational influence, advancing the use of cryogenics has become a strategic focus within the aerospace community [1,2]. Cryogenic Fluid Management (CFM) is now a top priority in NASA's plans to establish long-term habitats on the Moon and Mars, where cryogenic fluids are expected to play vital roles in both propulsion and thermal management, as illustrated in Fig. 1. A major current initiative in CFM technology is the development of cryogenic propellant depots in Low Earth Orbit (LEO).

The primary objective of cryogenic fuel depots in Low Earth Orbit (LEO) is to enable more ambitious deep space missions by limiting the amount of propellant launched from Earth to only what is required to reach orbit, with subsequent refueling occurring once in space. By shifting this additional propellant mass away from launch vehicles, mission capacity and duration can be significantly increased beyond what is currently achievable [3]. For a hypothetical spacecraft destined for regions beyond LEO, propellant transfer would occur from the

* Corresponding author at: .
E-mail address: mudawar@ecn.purdue.edu (I. Mudawar).
URL: http://engineering.purdue.edu/BTPFL (I. Mudawar).

https://doi.org/10.1016/j.ijheatmasstransfer.2025.127590
Received 18 May 2025; Received in revised form 3 July 2025; Accepted 23 July 2025
Available online 7 August 2025

Nomenclature

A	area [m^2]
a	gravitational acceleration [m/s^2]m/s^2]
c_p	specific heat [J /(kg·K)]
D	diameter [m]
D_j	diameter of vapor jet [m]
e_t	thermal effusivity, $\sqrt{k\rho c_p}$, $\left[W\sqrt{s}\ /\left(m^2K\right)\right]$
g	Earth gravitational acceleration, 9.81 m/s^2
H, H'	parameters in Haramura and Katto model
h_{fg}	latent heat of vaporization [J/kg]
K	coefficient in Haramura and Katto model
k	thermal conductivity [W /(m·K)]
L_c	characteristic length of heated surface [m]
N	number of datapoints
P	pressure [kPa]
P_c	critical pressure [Pa]
Pr	Prandtl number
q''	heat flux [W/m^2]
q''_{CHF}	critical heat flux [W/m^2]
$q''_{CHF,asy}$	asymptotic critical heat flux for infinitely large surfaces [W/m^2]
$q''_{CHF,EM}$	critical heat flux according to Tamvada et al. model [W/m^2]
$q''_{CHF,LD}$	critical heat flux according to Lienhard and Dhir model [W/m^2]
$q''_{CHF,ZK}$	critical heat flux according to Zuber-Kutateladze equation [W/m^2]
R_i	gas constant [J /(kg·K)]
R_q	root mean square (RMS) roughness [μm]
T	temperature [K]
T_{sat}	saturation temperature [K]
ΔT_{sub}	liquid subcooling, $T_{sat} - T_f$, [K]
u_g	vapor jet escape velocity [m/s]

Greek symbols

β	contact angle [°]
δ	heated wall thickness [m]
θ	angle of heated surface with respect to gravity (upwards normal = 0°)
κ	Liquid inflow factor in Haramura and Katto's model; κ = 0.83 is suggested
λ_d	Taylor most-dangerous wavelength [m]
λ_T	wavelength associated with onset of Taylor instability [m]
μ	dynamic viscosity [Pa·s]
ν	kinematic viscosity [m^2/s]
ρ	density $\left[kg/m^3\right]$
σ	surface tension [N /m]

Subscripts

CHF	conditions at CHF
EM	evaporation momentum
f	liquid
g	vapor
H	Helmholtz instability
j	vapor jet
LD	Lienhard and Dhir
meas	measured
pred	predicted
sat	saturation
sub	subcooling
T	Taylor instability
w	heated wall
ZK	Zuber-Kutateladze

Acronyms

AL	aluminum
CFM	Cryogenic Fluid Management
CHF	critical heat flux
FBCE	Flow Boiling and Condensation Experiment
LAr	liquid argon
LCH_4	liquid methane
LEO	low Earth orbit
LH_2	liquid hydrogen
LHe	liquid helium
LN_2	liquid nitrogen
LO_2	liquid oxygen
MAE	mean absolute error
NASA	National Aeronautics and Space Administration
OFHC	oxygen-free high conductivity copper
PU-BTPFL	Purdue University Boiling and Two-Phase Flow Laboratory
RMS	root mean square
SS	stainless steel

orbiting fuel depot to the client vehicle. However, refueling an empty cryogenic tank in orbit is a complex process, largely due to the two-phase phenomena associated with cryogenic fluid behavior in microgravity. Key challenges include chilldown of the transfer lines, self-pressurization [4] and chilldown of the receiving tank, and boil-off losses during long-term orbital storage. NASA researchers have conducted both modeling and experimental investigations to characterize these effects [5–7], and the need for higher-fidelity two-phase flow models has been widely recognized.

As a result, extensive efforts have been undertaken to characterize the phase change modes expected during tank-to-tank cryogenic transfer and long-term storage. Steady-state experiments, favored for their relatively low uncertainty, have been carried out both on the ground [8] and in short-duration parabolic flight simulating microgravity environments [9] using liquid nitrogen (LN_2) to study flow boiling and inform predictive models for transfer line operations. In addition, transient spray boiling experiments conducted onboard parabolic flights have demonstrated the feasibility of tank quenching under microgravity conditions [10]. To investigate two-phase thermal management in orbit, the International Space Station (ISS) has hosted the Flow Boiling and Condensation Experiment (FBCE), which examines long-term microgravity effects on heat transfer [11,12] and flow instabilities [13]. These studies aim to develop high-accuracy heat transfer coefficient correlations applicable across varying gravity levels.

A thorough understanding of the phase change phenomena associated with cryogenic fluids is essential for the development of predictable and well-controlled systems. Due to the distinct thermophysical properties of cryogens, room-temperature fluids are generally unsuitable as experimental analogues [14]. Nevertheless, predictive correlations have been successfully developed to unify the behavior of multiple cryogenic fluids across a range of conditions [15]. Based on this foundation, the present study employs LN_2 as the working fluid. LN_2 is an inert cryogen and has been demonstrated to serve as a suitable analogue for liquid oxygen (LO_2), a propellant of particular relevance to space applications [16].

During propellant tank filling, the accumulation of large liquid volumes becomes responsible for absorbing a significant portion of incoming heat. Over time, stored cryogens are subject to boil-off due to external heat ingress into the tank. Both propellant transfer and long-term storage phases can reasonably be modeled as undergoing pool

boiling. A key parameter in such scenarios is the critical heat flux (CHF), which indicates the transition away from (in heating scenarios) or toward (in quenching scenarios) nucleate boiling. Accurate prediction of CHF is crucial for system reliability and performance. Researchers at the Purdue University Boiling and Two-Phase Flow Laboratory (PU-BTPFL) have systematically studied CHF across a wide range of boiling modes using room-temperature fluids, including pool boiling [17], spray cooling [18], falling films [19,20], jets [21], flow boiling [22,23], capillary-driven flows [24], microchannels [25], and hybrid cooling strategies [26,27]. Building on this foundation, the present study aims to expand the cryogenic pool boiling CHF database and evaluate the applicability of existing predictive correlations for systems scaled to 'large' dimensions, beyond those previously explored in the literature.

1.2. Critical heat flux theory and mechanisms

In the heating regime of the boiling curve, there exists a critical point beyond which nucleate boiling can no longer be maintained under steady-state conditions. At this juncture, a sudden transition to film boiling occurs, characterized by a sharp and rapid rise in surface temperature. This phenomenon is known as the critical heat flux (CHF) and represents a fundamental safety limit. CHF is of particular importance to the design of thermal management systems, as exceeding this threshold can lead to significant degradation in heat transfer performance and potential system failure.

Zuber's hydrodynamic instability model [28] remains one of the most widely accepted theories for predicting CHF during saturated pool boiling on an infinite, horizontal flat plate. This model provides accurate predictions for a variety of fluids by attributing CHF to the onset of hydrodynamic instabilities that disrupt liquid supply to the heated surface as depicted in Fig. 2(a). Specifically, the model describes the formation of a vapor layer at the surface due to Taylor instability, followed by the emergence of vapor columns from the peaks of this layer. These columns eventually collapse, inhibiting further liquid access and leading to a rapid surface temperature rise. Zuber's theory incorporates the Kelvin–Helmholtz instability of wavelength λ_H at the liquid-vapor interface, which becomes prominent at high heat flux levels as vapor jets accelerate through the surrounding liquid. The resulting formulation, commonly referred to as the Zuber-Kutateladze equation, is expressed as:

$$q''_{CHF,ZK} = \frac{\pi}{24}\rho_g h_{fg}\left[\frac{\sigma g(\rho_f - \rho_g)}{\rho_g^2}\right]^{1/4} \tag{1}$$

In his formulation, Zuber proposed that the characteristic wavelength of the vapor layer corresponds to the Taylor "most dangerous" wavelength (λ_d), which is defined as:

$$\lambda_d = 2\pi\sqrt{3}\left[\frac{\sigma}{g(\rho_f - \rho_g)}\right]^{1/2} \tag{2}$$

Lienhard and Dhir [29] proposed replacing Zuber's depiction of the one-dimensional Taylor wavelength with a more accurate three-dimensional spacing of $\sqrt{2}\lambda_d$, which accounts for the arrangement of repeated planar cells spanning the heated surface. This modification culminated in a higher predicted CHF for saturated pool boiling on an 'infinitely large' horizontal surface, offering improved agreement with experimental data.

$$q''_{CHF,LD} = 1.14\ q''_{CHF,ZK} \tag{3}$$

Lienhard et al. [30] further investigated the limitations of Zuber's model by examining its implicit assumption of an "infinitely large" horizontal surface. They demonstrated that deviations from the model arise when the heated surface does not sufficiently approximate this condition. As shown in Fig. 2(b), finite surfaces give rise to large liquid eddies within the otherwise quiescent pool, induced by the continuous stream of vapor escaping from the surface. This recirculating flow can disrupt the regular vapor column formation predicted by the model. For surfaces that fall below the threshold of the 'infinitely large' criterion, this disruption alters the CHF mechanism and can result in a higher measured q''_{CHF} than predicted. The cutoff for avoiding size-related effects was determined to be approximately three times the most dangerous Taylor wavelength ($3\lambda_d$), a length sufficient to sustain a central vapor column that collapses in accordance with the model's assumptions.

For flat heated surfaces that cannot be considered infinitely large, Tamvada et al. [31] developed a critical heat flux (CHF) model based on the evaporation momentum (EM) theory originally proposed by Steinchen and Sefiane [32], proposing the following relation for the evaporation momentum CHF, characterized as the hydrodynamically stable boiling limit:

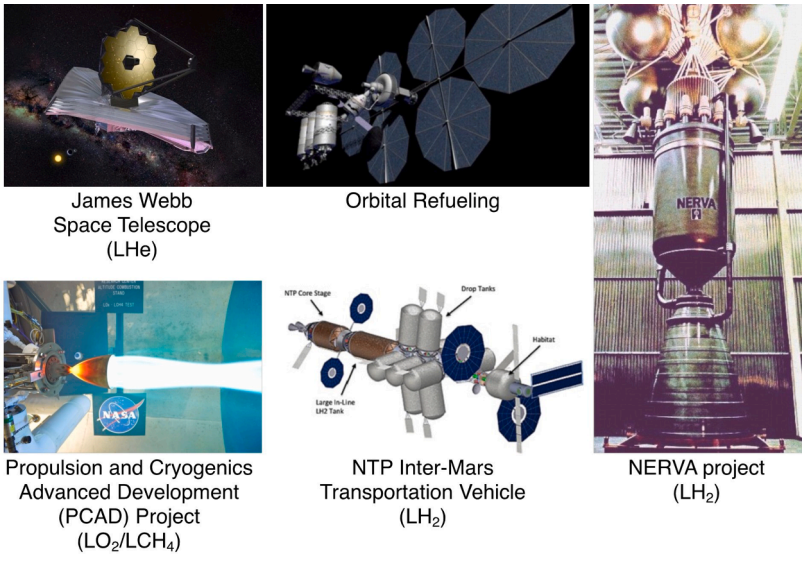

Fig. 1. Space applications of cryogens.

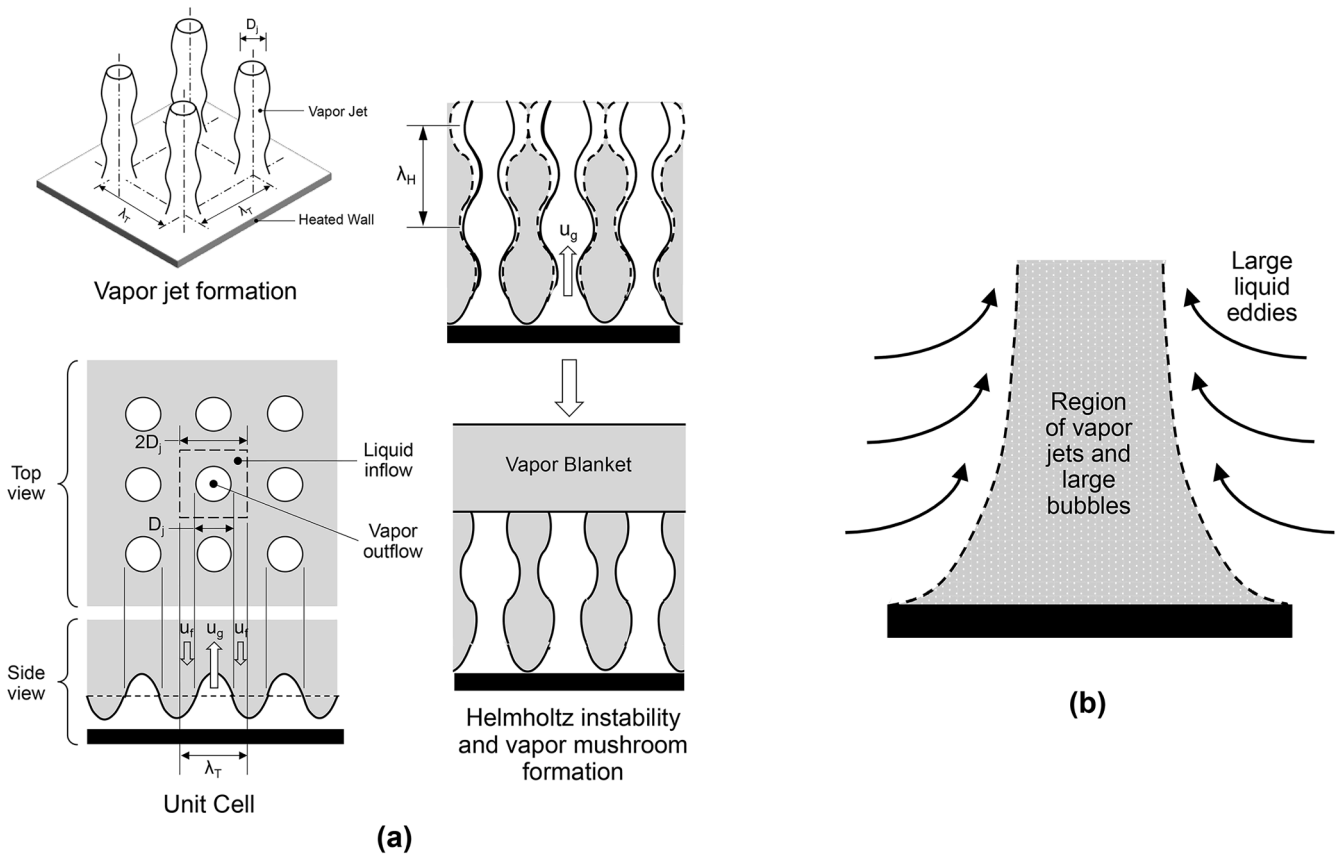

FIG. 2. (a) Schematic representation of Zuber's hydrodynamic instability model for an infinite horizontal heated surface. (b) Modified CHF mechanism for short heaters due to large liquid eddies.

$$q''_{CHF,EM} = \rho_g h_{fg}\left[\frac{\sigma g(\rho_f-\rho_g)}{\rho_g^2}\right]^{1/4}\frac{(1+cos\beta)}{[3\pi^2]^{1/4}}\left[\frac{\pi-\beta+cos\beta}{\pi-\beta+\frac{sin2\beta}{2}}\right]^{1/2} \quad (4)$$

This model, which incorporates the effect of contact angle β, postulates that for very small horizontal surfaces (specifically those smaller than the fluid's capillary length) undergoing nucleate boiling, a vapor pocket forming on the surface can grow unbounded, eventually encapsulating the entire heated area under a thin vapor film. This occurs when the evaporation momentum forces, which promote lateral growth of the vapor pocket, exceed the restraining surface tension forces. Tamvada et al. experimentally demonstrated this behavior for water, ethanol, and FC-72, showing a clear dependence of the CHF on the size of the heated surface. Their results revealed that CHF is constrained between two limits: the hydrodynamic stability limit governed by evaporation momentum, and the hydrodynamic instability threshold characterized by the $3\lambda_d$ criterion.

For liquid nitrogen (LN_2) at atmospheric pressure, the $3\lambda_d$ threshold corresponds to 34.7 mm, which is approximately one-third the length of the heated surface used in the present experimental investigation. As discussed in a later section, this satisfies the criterion for an effectively infinite surface size. Interestingly, a review of the historical database compiled by Patel et al. [15] reveals that the vast majority of previously tested heated surfaces fall below this cutoff size. As a result, the CHF mechanism in those studies is likely governed by different physics than what is predicted by infinite surface models.

1.3. Heated surface material and thickness effects

It is widely recognized across a range of working fluids that the material of the heated surface plays a significant role in influencing the onset of CHF instability [33,34]. However, the underlying physical mechanisms responsible for this variability remain a topic of ongoing debate. Several material properties have been proposed to correlate with observed experimental trends, including surface thermal conductivity (k_w), specific heat capacity ($c_{p,w}$), and density (ρ_w).

This trend has also been observed in boiling with cryogenic fluids [35], where experiments demonstrated a degradation in CHF across different heated surface materials. These results suggest a dependence on the surface's thermal effusivity, defined as:

$$e_{t,w} = \sqrt{k_w \rho_w c_{p,w}} \quad (5)$$

These studies report substantial degradation in q''_{CHF} for stainless steel heated surfaces compared to copper. Recently, Bombardieri and Manfletti [36] investigated the effect of wall material on saturated pool boiling CHF on a horizontal surface using liquid nitrogen (LN_2) as the working fluid. Their experiments employed relatively large square heaters, each with a characteristic length of 46 mm, made from copper, aluminum, and stainless steel. The results showed significant reductions in CHF: 59% for aluminum and 42% for stainless steel, both relative to copper. The thermal conductivities of these materials, which are central to interpreting these results, are presented in Fig. 3.

Bar-Cohen and McNeil [37] employed the concept of thermal effusivity to analyze the impact of heated surface thickness on CHF performance. They found that sufficiently thick surfaces exhibit little sensitivity to thickness, while thin surfaces demonstrate a notable reduction in CHF. To quantify this effect, they introduced a correlation relating the CHF of thin heaters, q''_{CHF}, to that of sufficiently thick heaters, referred to as the asymptotic CHF limit, $q''_{CHF,asy}$ across various materials:

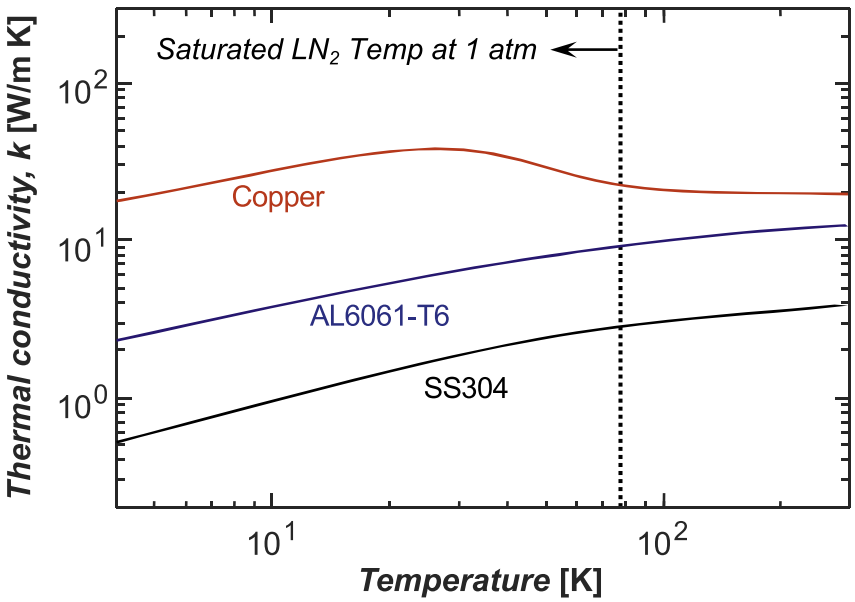

Fig. 3. Variation of thermal conductivity with temperature for different engineering materials. Properties obtained from NIST.

$$\frac{q''_{CHF}}{q''_{CHF,asy}} = \frac{\delta\, e_{t,w}}{\delta\, e_{t,w} + 0.8\ [m{\cdot}K/W\sqrt{s}\,]} \tag{6}$$

where δ is the heating surface thickness. This formulation effectively captures the coupled effects of heating surface material properties and thickness. According to the correlation, the CHF reaches 90% of its asymptotic value when the dimensionless parameter $\delta\, e_{t,w} = 8$, and 99% when $\delta\, e_{t,w} = 85$. As shown in Eq. (6), the asymptotic CHF limit is effectively achieved when the wall thickness exceeds approximately 0.22, 0.34, and 1.1 mm for copper, aluminum, and stainless steel, respectively, beyond which further increases in thickness have a negligible effect on CHF.

Similarly, Stephan and Abdelsalam [38] incorporated the thermal effusivity of the heated surface into their CHF correlation but normalized it by the thermal properties of the working fluid to enhance universality across different fluid–surface combinations.

Importantly, thermal system designers often rely on well-known CHF correlations developed for infinitely large surfaces, without accounting for the thermal properties or thickness of the heated wall. This practice can be problematic, as it may lead to overestimation of the actual CHF, thereby increasing the risk of burnout or even permanent system failure.

1.4. Prior relevant cryogenic pool boiling research and objectives of current study

Cryogenic pool boiling critical heat flux (CHF) has been a topic of sustained interest for several decades, primarily due to the use of cryogenic fluids in aerospace systems. In recent years, interest has been renewed as cryogenic fluid management (CFM) technologies continue to evolve. Beginning in the 1950s and 1960s, experimental investigations into cryogenic pool boiling matured, alongside the development of predictive tools and models that became benchmarks for the field. Focusing specifically on liquid nitrogen (LN_2), early experiments such as those conducted by Kosky [39] demonstrated that CHF increases with operating pressure, consistent with trends observed in room-temperature fluids. This increase persists up to a reduced pressure of approximately 0.4, beyond which CHF begins to decline as the system approaches the fluid's critical pressure. More recent studies have shifted toward advanced diagnostics and performance enhancement. These include high-resolution measurement techniques (e.g., shadowgraphy and infrared thermography) [40], detailed analyses of bubble dynamics [41], and surface engineering strategies to enhance CHF through microscale surface modifications [42].

The primary objective of this study is to expand the cryogenic pool boiling CHF database, with particular emphasis on parameters that have been insufficiently addressed in prior literature. The novel experimental approach presented here involves the use of a variety of working surface materials and multiple operating pressures, applied to surfaces significantly larger than those previously studied. To guide this investigation, the historical database of flat-surface cryogenic pool boiling CHF experiments compiled by Patel et al. [15] is leveraged to contextualize the effects of key parameters. Specifically, this study examines three heated surfaces, each with a characteristic length, L_c, of 10.11 cm, which exceeds the estimated threshold for achieving asymptotic CHF. These surfaces are constructed from commonly used engineering materials: copper, aluminum, and stainless steel. In contrast, over 90% of the LN_2 CHF data points in [15] correspond to surface sizes smaller than 4 cm, and 68% involve either copper or platinum heaters. When considering all cryogenic fluids represented in the database, over 87% of data points are for surfaces smaller than 3 cm, with 78% derived from copper or platinum heaters. These trends underscore the limited diversity in both surface size and material historically explored. Accordingly, this study addresses these gaps by generating new CHF data under varied material and geometric conditions, with the aim of informing the development of a more comprehensive and universal cryogenic CHF correlation that accurately captures the observed trends.

2. Experimental methods

2.1. Experimental cryogenic pressure chamber

To investigate cryogenic two-phase heat transfer, an experimental apparatus was constructed that could maintain pressurized liquid nitrogen (LN_2) while also allowing for modular design and accessible instrumentation. This was achieved by using sanitary Tri-Clamp stainless steel cylinders to form the walls of the pressure vessel. The central section of the chamber was modified to include viewports, while the top and bottom sections incorporate jacketed insulation for thermal stability. Fig. 4 shows schematics of the pressure chamber and heater assembly. As illustrated, flanges at the top and bottom of the chamber provide ports for instrumentation, liquid nitrogen feed, and pressure regulation. Inside the chamber, a stainless-steel pedestal extends

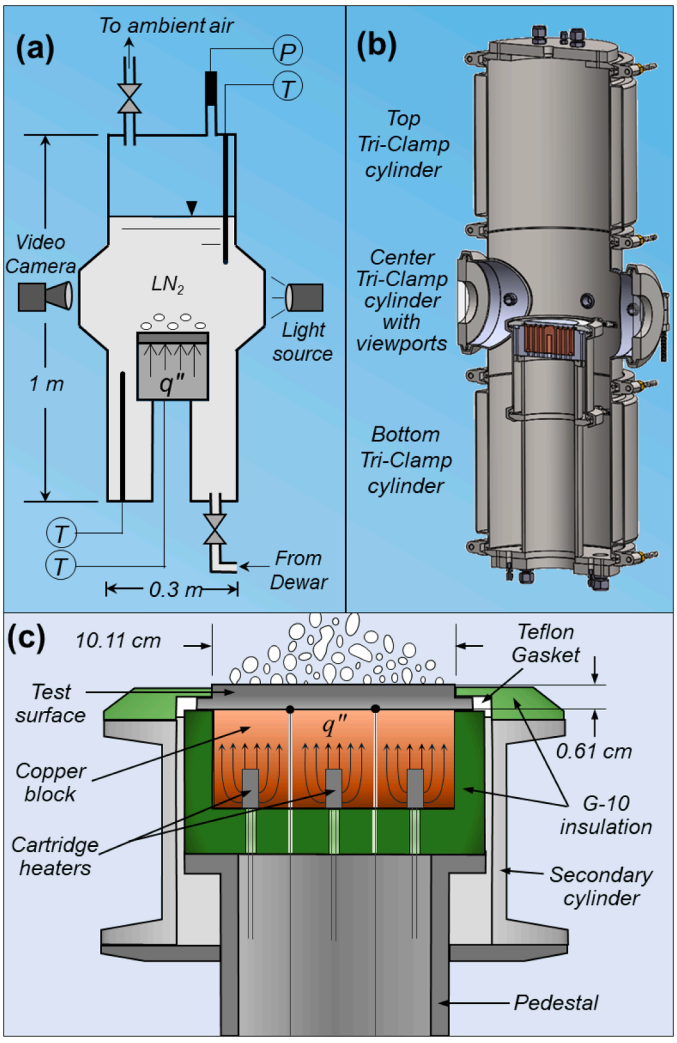

Fig. 4. Experimental cryogenic chamber: (a) schematic of chamber plumbing and instrumentation, (b) CAD model of chamber assembly, and (c) schematic of heater assembly.

upward from the bottom flange to a point just below the viewport, serving as a mounting platform and feedthrough for power and instrumentation connections to the heated test surface assembly.

The cryogenic pressure chamber has a liquid capacity of 40 L and is rated for operation up to 517 kPa, as determined by hydrostatic testing performed at room temperature. For safety, all experiments were conducted within a pressure range of 101 to 448 kPa. The liquid pool temperature and system pressure were monitored using sensors mounted on the chamber flanges, as shown. Measurement uncertainties were ±0.5°C for temperature and ±0.25% for pressure.

2.2. Test surface and heater assembly

To meet and exceed the $3\lambda_d$ threshold established by Lienhard et al., the heater was designed to deliver uniform heat across large surfaces of varying materials. As shown in Fig. 4(c), the heater assembly consists of several cartridge heaters embedded within a large copper block, housed in an insulating G-10 cradle. The test surface is bonded to the opposite end of the copper block using a thermally conductive boron nitride epoxy and clamped to a secondary stainless-steel cylinder via a G-10 flange. Power is supplied to the cartridge heaters through a variable voltage transformer and monitored with a Yokogawa digital wattmeter, which has a power measurement accuracy of ±0.5%. The uniform heat flux assumption was made by developing a steady-state conduction model using Ansys Fluent to ensure that the thickness of the copper block was sufficient to diffuse the input from the cartridge heaters, and that the thickness of each heated surface would be sufficient to diffuse gradients arising from the instrumentation thru-holes.

Type E thermocouples, welded to the backside of the test surface, pass through the copper block, continue downward through the pedestal, and exit the chamber. The thermocouple welds are made on the bottom of the heated surface using a capacitive discharge welder, ensuring both accurate temperature readings and secure attachment. The test surface includes a small lip to facilitate sealing with a Teflon gasket and is mounted so that only the front face is exposed to the liquid pool. An annular space within the secondary cylinder provides an additional layer of thermal insulation between the heater and the liquid pool, minimizing heat loss from the heater assembly. An assembly-level system checkout was performed by measuring the heated surface top-side and bottom-side temperatures at different axial and circumferential positions to ensure minimal deviation in readings on either side, thereby validating the uniform heat flux assumption.

Three different test surfaces were used in the experiments, each made from a distinct material: 304 stainless steel, 6061-T6 aluminum, and oxygen-free high thermal conductivity (OFHC) copper, as shown in Fig. 5(a). These materials were chosen to represent both commonly used aerospace materials for cryogenic thermal management and materials less frequently studied in the existing literature. Each test surface has a minor diameter of 101.1 mm, which is nearly three times the $3\lambda_d$ threshold, thereby satisfying the infinite plate assumption. The test surfaces are designed to have sufficient depth, 6.1 mm, so as to ensure degradations in CHF are not observed resulting from minimized thickness effects [35]. To ensure consistency in surface characteristics, all test surfaces underwent identical treatments to achieve a realistic engineering surface finish. A prescribed root mean square (RMS) roughness, R_q, was applied, with measurements taken using an optical profilometer confirming R_q of 0.6 μm. Fig. 5(b) shows the fully assembled test heater and heater block, while Figs. 5(c) and 5(d) display, respectively, the heater assembly mounted atop the pedestal and the fully assembled test chamber covered with Cryogel Insulation.

2.3. Visualization capabilities

The middle cylinder of the pressure chamber was modified to include two viewports positioned 180° apart, as shown in Figs. 4(a) and 4(b), allowing continuous visual monitoring of surface boiling conditions throughout each experiment. Each viewport consists of a 7.62-mm thick borosilicate glass disk fused to a stainless-steel flange. Visual observation serves to validate interpretations based on temperature data collected during testing and provides qualitative insight into nucleation behavior leading up to the onset of film boiling at critical heat flux (CHF).

High-speed videography was employed to capture these phenomena using a Photron Fastcam Ultima APX camera, positioned facing one of the viewports and recording at 1000 frames per second (fps). Illumination was provided by an Arrilux Pocketpar lamphead positioned facing the opposite viewport to ensure clear visibility of boiling behavior.

2.4. Experimental procedure

A systematic procedure was carefully developed for operating the pressure chamber to ensure controlled and repeatable experimental conditions. LN_2 is supplied from a high-pressure (~1.4 MPa) storage dewar to a lower-pressure transfer dewar (200 kPa), which is used for chilling down the system, charging the chamber, and maintaining the desired liquid level during testing. The filling process begins with a one-hour near-atmospheric purge using cold nitrogen vapor to displace ambient air from the system. This is followed by a gradual introduction of LN_2 over an additional hour, during which the system pressure is maintained below 140 kPa. The transfer of LN_2 from the dewar to the

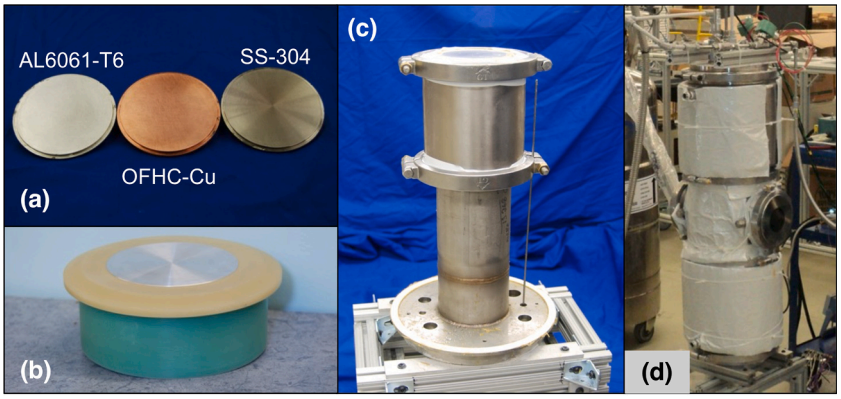

Fig. 5. Photographs of (a) aluminum 6061-T6, oxygen free copper, and 304 stainless steel heated surfaces used in experimentation, (b) heater module assembly in G-10 insulation, (c) pedestal with heater module installed, and (d) fully assembled chamber.

chamber is carefully regulated using high-pressure nitrogen vapor to control flow rate. Liquid is introduced until the level reaches approximately 300 mm above the test surface. At this point, system pressure is either increased or decreased to the desired experimental setpoint. Throughout the process, the test surface temperature is closely monitored to verify a proper chilldown thermal response, and visual confirmation is performed to ensure the absence of boiling prior to the initiation of the experiment.

Once the thermocouples embedded in the test surface reach the prescribed saturation temperature, the experiment begins with a gradual increase in heater power. Power is initially raised in 10% increments relative to the expected CHF until approximately 50% of the expected CHF is reached. Beyond this point, power is increased in smaller 5% increments to allow finer resolution approaching CHF. At each power step, the system is allowed to reach thermal equilibrium, defined as a temperature change of less than 0.1 K over a 30-s period. The time required to reach steady-state conditions varied significantly depending on the test surface material. For stainless steel, the least thermally conductive material tested, thermal convergence could take up to 30 min. In contrast, for highly conductive copper, convergence was typically achieved within a few minutes. Throughout the test, chamber pressure is actively maintained within ±3.5 kPa of the setpoint by venting excess nitrogen vapor generated during boiling. Power increments continue until a sudden temperature excursion is observed, indicating the onset of CHF. The reported CHF value is taken as the average heat flux of the final two increments. This approach accounts for

Table 1
Summary of relevant and seminal CHF correlations assessed in the current study.

Author(s)	Model or Correlation
Patel et al. [15]	$q''_{CHF} = \left[0.16 - 0.104\left(\frac{P}{P_c}\right)^{10}\right]\left[1 - 0.004\left(\frac{P}{P_c}\right)\theta\right]\left\|cos\left(\left(\frac{88}{180}\right)\theta\right)\right\|^{0.364} \times \left[1 + 0.16\left(\frac{c_{p,f}\Delta T_{sub}}{h_{fg}}\right)\right]\left[\rho_g h_{fg}\left(\frac{\sigma g(\rho_f - \rho_g)}{\rho_g^2}\right)^{1/4}\right]\left[\frac{a}{g}\right]^{0.17}$
Lienhard & Dhir [30]	$q''_{LD} = 0.149\rho_g h_{fg}\left[\frac{\sigma g(\rho_f - \rho_g)}{\rho_g^2}\right]^{1/4}$
Li et al. [45]	$q''_{CHF} = \left[0.1272 - 0.13\left(\frac{P}{P_c}\right)^{7.7}\right]\left(1 + \frac{Pr_g}{Pr_f}\right)^{0.5}\left[1 - 0.00075\,\theta\left(\frac{P}{P_c}\right)\left(\frac{Pr_g}{Pr_f}\right)^6\right] \times [1 - 0.0007\,\theta\,tan(0.427\theta) - 0.1138\,sin(0.292\theta)]\left[1 + 0.0032\,\theta\left(\frac{c_{p,f}\Delta T_{sub}}{h_{fg}}\right)\right] \times \left[1 + 0.0554\left(\frac{c_{p,f}\Delta T_{sub}}{h_{fg}}\right)\right]\left[\frac{a}{g}\right]^{0.15}\rho_g h_{fg}\left[\frac{\sigma g(\rho_f - \rho_g)}{\rho_g^2}\right]^{1/4}$
Haramura & Katto [46]	$q''_{CHF} = K\left[0.721\left(\frac{A_g}{A_w}\right)^{5/8}\left(1 - \frac{A_g}{A_w}\right)^{5/16}\left[\left(\frac{\rho_f}{\rho_g} + 1\right)/\left(\frac{11}{16}\frac{\rho_f}{\rho_g} + 1\right)^{3/5}\right]^{5/16}\rho_g h_{fg}\left[\frac{\sigma g(\rho_f - \rho_g)}{\rho_g^2}\right]^{1/4}\right]$ where $A_g/A_w = 0.0584\,(\rho_g/\rho_f)^{0.2}$ and $K = \begin{cases} 1 \text{ for infinite surface} \\ \left[\left(\frac{\sqrt{3}\pi}{H'}\right)^{1/16}\left[1 + \frac{1}{2}\left(\frac{\pi}{H'}\right)^2\right]^{1/32}\right] \text{ for vertical oriented ribbon} \\ \left[(1+\kappa)^{5/16}\left[3^{1/2}2\pi\left(\frac{\sigma}{g(\rho_f - \rho_g)}\right)^{1/2}\right]/\left(\frac{\pi}{4}L_c^2\right)^{1/16}\right] \text{ for small disk} \end{cases}$ where $H' = H/\left[\sigma/g(\rho_f - \rho_g)\right]^{1/2}$
Yagov [47]	$q''_{CHF,l} = 0.5\,\frac{h_{fg}^{81/55}\sigma^{9/11}\rho_g^{13/110}k_f^{7/110}g^{21/55}f(Pr_f)}{\nu_f^{1/2}c_{p,f}^{3/10}R_i^{79/110}T_{sat}^{21/22}}$ for $P/P_c < 0.001$ where $f(Pr_f) = \left(\frac{Pr_f^{9/8}}{1 + 2\,Pr_f^{1/4} + 0.6\,Pr_f^{19/24}}\right)^{4/11}$ $q''_{CHF,h} = 0.06h_{fg}\rho_g^{3/5}\sigma^{2/5}\left[g(\rho_f - \rho_g)/\mu_f\right]^{1/5}$ for $P/P_{crit} > 0.03$ $q''_{CHF} = \left(q''^3_{CHF,h} + q''^3_{CHF,l}\right)^{1/3}$ for $0.001 < P/P_{crit} < 0.03$

the fact that the actual CHF lies between the last steady-state nucleate boiling point and the step that triggers the transition to film boiling. The reported system pressure corresponds to the time-averaged pressure recorded during the final steady-state step prior to CHF.

3. Experimental results & discussion

3.1. CHF data trends

Given the sparsity of data in the literature and its resistance to oxidation, 304 stainless steel (SS304) was selected as the initial surface for characterization. CHF experiments were conducted over a pressure range of 101–517 kPa. At atmospheric pressure, the measured CHF was nearly half of the value predicted by the CHF correlation developed specifically for cryogenic fluids by Patel et al. [15] (see Table 1). As shown in Fig. 6, CHF increased linearly from 101 to 350 kPa before gradually leveling off. This trend is consistent with other cryogenic CHF studies [43] and aligns with the general form of existing CHF correlations at elevated pressures. At low pressures, CHF increases rapidly for increases in P_{sat} due to the enhanced surface rewetting from decreased bubble departure diameters and increased bubble departure frequency. As the critical pressure is approached, however, distinction between liquid and vapor phases begins to decrease, and as a result the critical heat flux begins to plateau and eventually decreases towards zero at P_{crit}. Due to the limited availability of SS304 data in the literature, it was initially hypothesized that the observed disparity in CHF magnitude with respect to the Patel correlation was due solely to the surface material, specifically the low thermal conductivity of stainless steel. To test this hypothesis, the heated surface material was changed, which ultimately helped reveal a second mechanism influencing the onset of CHF.

Testing with AL6061-T6 further clarified the influence of material properties, consistently demonstrating a higher CHF compared to SS304 under identical operating conditions. As shown in Fig. 6, experiments conducted over the 101–380 kPa range revealed the same general trend of increasing CHF with rising system pressure, similar to that observed for SS304. However, the measured CHF values remained below those predicted by cryogenic correlation. To further validate the consistency of the experimental dataset, a copper surface was also tested. As shown in Fig. 6, CHF values for copper, while still lower than correlation predictions, exceeded the values recorded for both AL6061-T6 and SS304.

3.2. Material effect on CHF

Fig. 6 demonstrates that CHF for the three tested heated surface materials follows a consistent trend with increasing pressure, also closely aligning with the trend predicted by the Patel et al. [15] correlation. However, a notable degradation in CHF is observed for the AL6061 and SS304 surfaces compared to copper. Given that all other operating conditions are held constant, these differences can be attributed to the intrinsic properties of the heating surface materials, particularly considered is the thermal conductivity, which is highest for copper, followed by AL6061, and then SS304, as is also reflected in Fig. 6. Overall, it can be concluded that metallics with lower thermal conductivity are more prone to CHF at lower heat fluxes. The thermal conductivity is considered the primary parameter by which to characterize the material effect on CHF (as opposed to thermal diffusivity or effusivity) because the cause of temperature surge can be attributed to the differences in pseudo-steady-state planar temperature distribution between varied surfaces caused by the disparities in thermal conductivity. Higher overall surface temperatures in the steady state can be inferred to give rise to otherwise earlier critical heat flux.

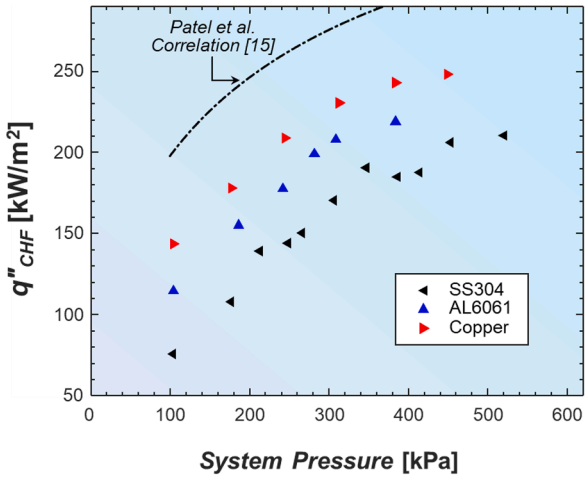

Fig. 6. Variation of measured CHF for saturated LN_2 pool boiling from a horizontal surface with system pressure for three tested heated surface materials.

The physical basis for this trend lies in the transient conduction dynamics within the heated surface. Materials with lower thermal conductivity are less effective at facilitating lateral heat conduction from regions of poor local cooling to adjacent areas with more effective cooling. This limitation has been shown to reduce nucleation site density, increase bubble waiting times, and result in greater temperature fluctuations within the bubble macro-region [44]. Regarding its impact on CHF, the reduced thermal conductivity impairs the redistribution of heat from surface areas beneath the troughs of the Taylor vapor wave to those beneath the vapor jets. This limitation intensifies lateral temperature gradients across the surface, leading to elevated surface temperatures in the wave troughs, particularly for materials with lower thermal conductivity, leading to earlier CHF commencement.

3.3. Visualization findings

The visualization capabilities of the experimental test chamber allowed for high-speed video capture of the CHF event, as illustrated in Fig. 7. As the heat flux is incremented to its final step, the surface temperature initially rises gradually, with high heat-flux nucleate boiling persisting, as shown in the upper image, designated as CHF-, the moments leading up to transition. The high heat flux boiling regime is recognized by high-speed coalescent vapor plumes manifesting from bubble merging presumed to be taking place between neighboring nucleation sites and bubble formations as they depart the surface. The vapor amalgamation is compressed and maintained near to the center of the surface as it departs due to the presence of liquid eddies induced by the continuous stream of vapor within the otherwise quiescent liquid pool. Once nucleate boiling can no longer be sustained, however, the surface undergoes a rapid transition, marked by a dramatic increase in the rate of temperature rise. Due to slightly improved cooling from better liquid access along the outer periphery of the heated surface, dryout initiates near the center and spreads radially outward. Following the transition at CHF+, the entire surface becomes encapsulated by a thin vapor layer, signaling the onset of film boiling, a regime characterized by the formation of much larger vapor bubbles and sustained at a significantly higher wall superheat. Film boiling is recognized by the formation of distinctive mushroom cap vapor bubbles which emanate from a thin oscillatory vapor layer, as seen in the lower image.

As will be discussed in the following section, it can be expected that as the diameter of the heated surface decreases, the relative contribution of more effective cooling along the periphery (as compared to the central region) increases, especially for very small diameters, thereby delaying the onset of CHF to higher values. It is surmised that the overall lower CHF values observed for the present heated surfaces, relative to the predictions of the Patel et al. correlation which is primarily based on a historical database of smaller surface areas, can be attributed to the significantly larger heated surfaces employed in this study. In fact, the CHF transition must necessarily occur in the center based on the findings of Lienhard and Dhir [30], where unstable departing vapor columns in

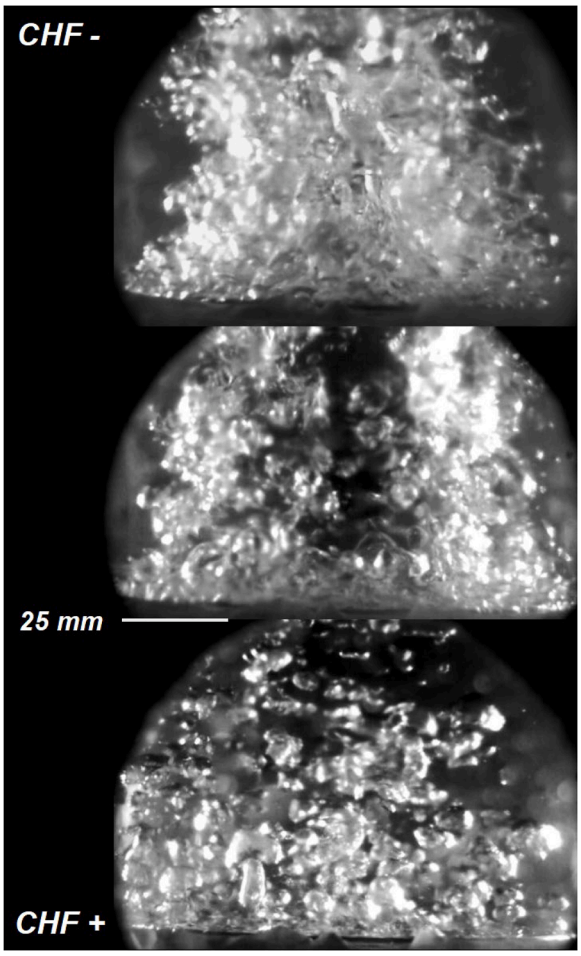

Fig. 7. Visualization of the development of CHF following the final heat flux increment. From left to right: nucleate boiling just prior to temperature excursion (*CHF* -), evolution of boiling regime during temperature excursion, and establishment of film boiling as temperature stabilizes (*CHF* +).

the center are shielded by those along the periphery.

3.4. Heated surface size in present study versus historical database

Taking into account the influence of heater size, as proposed by Lienhard and Dhir [30], Fig. 8 presents both the current experimental results and a compilation of historical CHF data for LN_2 from horizontal surfaces at atmospheric pressure. The data are plotted against the non-dimensionalized heater size, L_c/λ_d, and segregated for copper, aluminum, and stainless-steel surfaces. It is evident that a significantly larger body of historical data exists for copper, with comparatively fewer data points available for aluminum, and even fewer for stainless steel. Fig. 8 illustrates that CHF decreases with increasing heater size, eventually reaching a plateau for surfaces with a characteristic length greater than $\sim 3\lambda_d$, consistent with the findings from [30]. Such surfaces can be considered 'infinitely large' in the context of CHF behavior.

As the size of the heated surface increases, the inner vapor columns can be sustained by nucleation activity and enhanced liquid cooling near the outer periphery. This causes the onset of CHF, to originate from the center of the surface. For a comparatively smaller surface, the central Taylor-Helmholtz instability pattern is highly disrupted by peripheral liquid recirculation, resulting in a higher CHF. This highlights a key limitation in existing state-of-the-art CHF correlations, which are predominantly based on data from small heaters that do not meet the infinite plate criterion. Consequently, these correlations tend to over-predict CHF for larger surfaces. It is therefore essential, particularly in the design of cryogenic fluid management systems, to recognize this discrepancy and to develop new predictive models that account for this size-dependent behavior.

4. New correlation development

4.1. Assessment of prior correlations

To evaluate the performance of prior predictive tools, the most reliable correlations for cryogenic CHF, as identified by Patel et al. [15], were assessed and compared against the experimental CHF results obtained in this study. These correlations fall into three categories: those developed specifically for cryogenic fluids [15,45], those incorporating size effects consistent with the observations of this study [30,46], and those originally derived for room-temperature fluids but shown to provide reasonable predictive accuracy for cryogens [30,47]. The mathematical form of each correlation is summarized in Table 1. To quantify the accuracy of each correlation relative to the current experimental data, the mean absolute error (MAE) will be used as the primary metric.

$$MAE = \frac{1}{N}\sum \frac{\left|q''_{CHF,pred} - q''_{CHF,meas}\right|}{q''_{CHF,meas}} \times 100 \tag{7}$$

Fig. 9 presents parity plots that visualize the performance of the selected correlations against the experimental data from this study. The best-performing correlation is that of Haramura and Katto, which incorporates surface size effects and yields a MAE of 24.85%. Notably, it is also the only correlation that tends to underpredict the experimental results. The next best is Yagov's correlation, with an MAE of 37%. The cryogenics-optimized correlations by Patel et al. and Li et al. show comparable performance, with MAEs of 55.9% and 49.8%, respectively. Similarly, the correlation by Lienhard and Dhir yields a MAE of 45.18%. These findings underscore the need to develop a new CHF correlation that more accurately captures the behavior observed in the present experimental dataset.

4.2. Development of new cryogenic CHF correlation

To further generalize and improve the predictive capability of cryogenic pool boiling CHF correlations, the correlation proposed by Patel et al. is augmented with two additional parameters and a modified reduced pressure term. These new parameters are introduced to account for the two key influences identified in this study that significantly impact the onset of CHF: the heater's characteristic length and its material properties. As demonstrated in the preceding sections, both factors exhibit distinct and consistent trends with respect to CHF behavior, warranting their explicit inclusion in the predictive framework.

In order to capture the effect of heater size, the dimensionless length for a given heater is made the operating variable within an exponential decay function. This parameter accounts for the degradation in CHF as the surface size increases but is offset so as to plateau at a finite value. The effect of surface material is captured using the wall's thermal conductivity, normalized by the same for the fluid. It is noted that wall thermophysical properties are taken at the liquid saturation temperature. The final correlation with additional parameters takes the form:

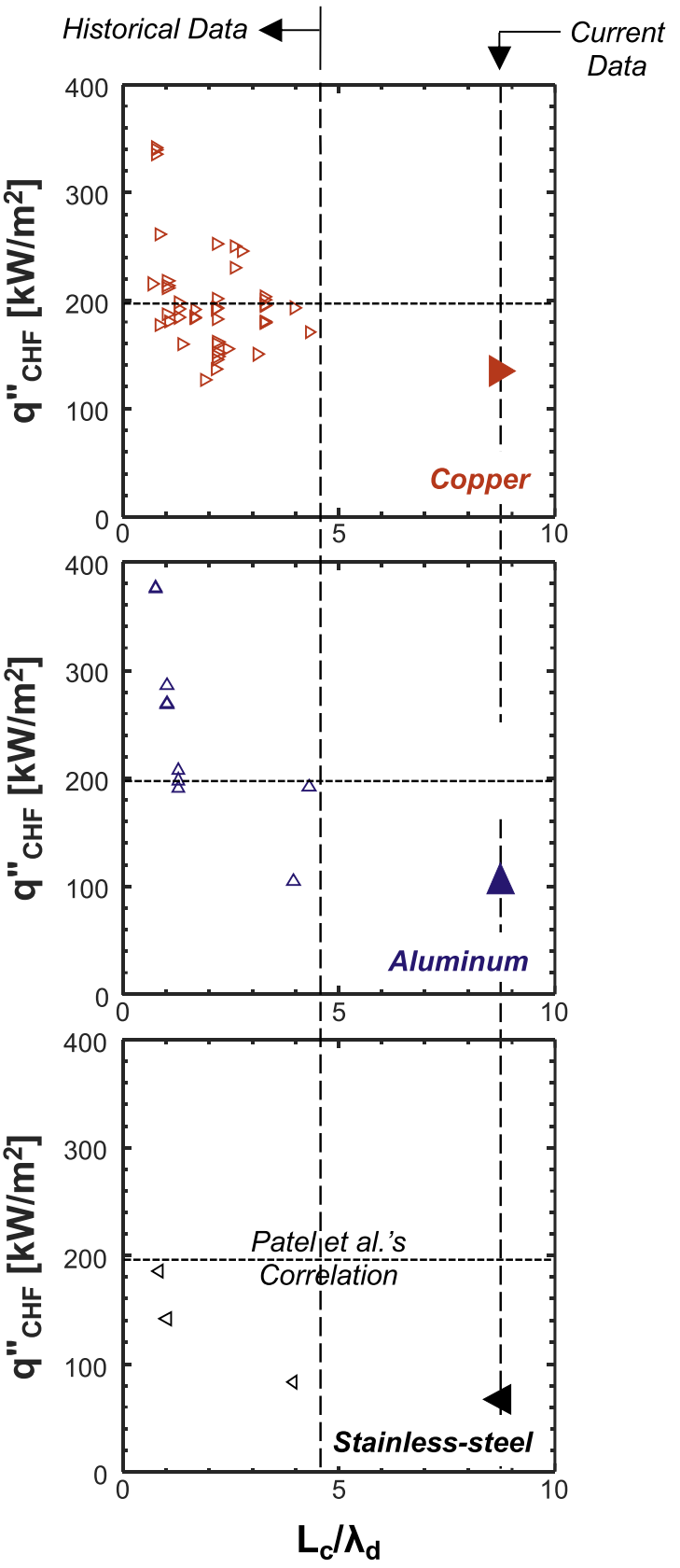

Fig. 8. Current CHF experimental results for LN_2 from horizontal surfaces at atmospheric pressure compared to historical data compiled by Patel et al. [15].

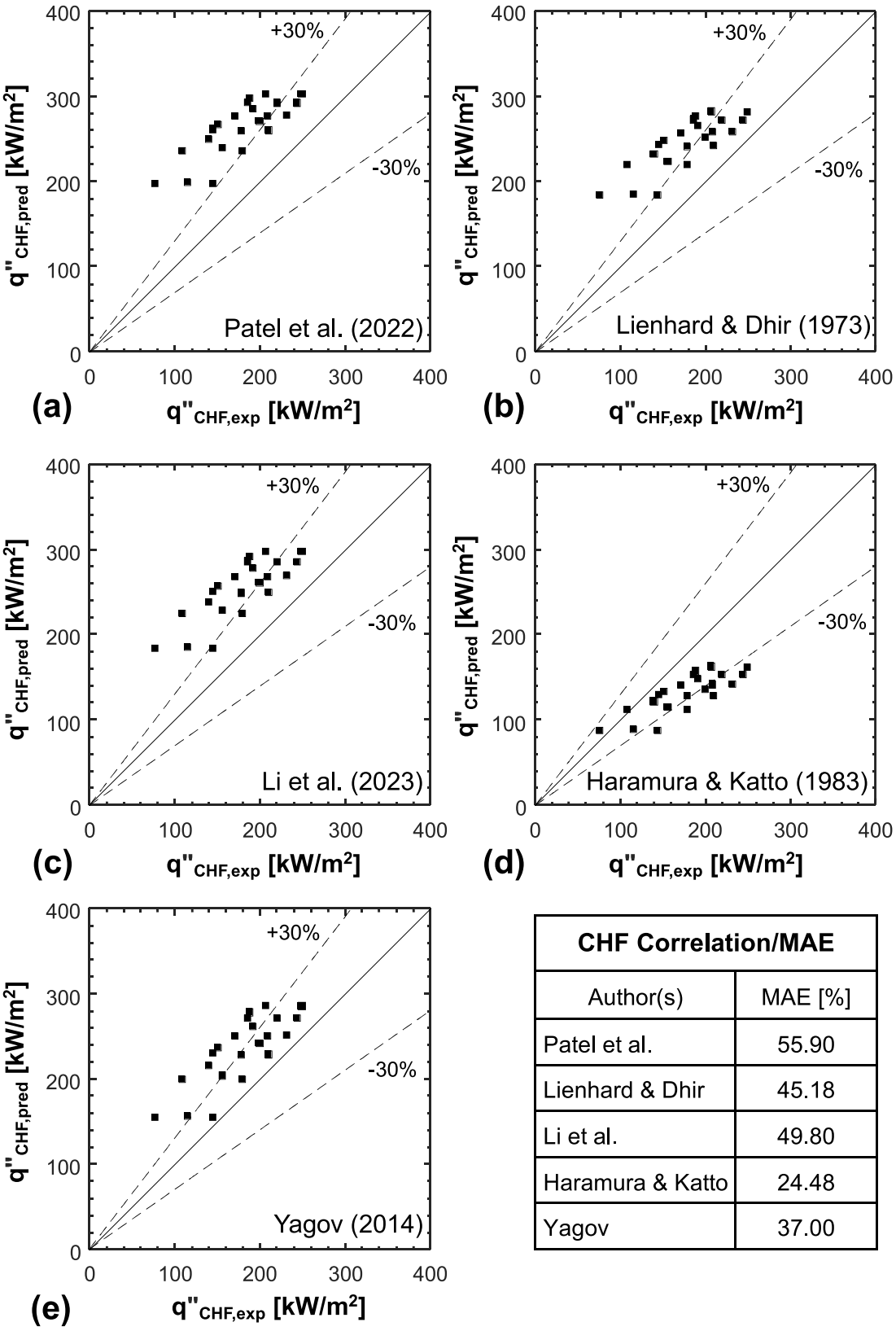

CHF Correlation/MAE	
Author(s)	MAE [%]
Patel et al.	55.90
Lienhard & Dhir	45.18
Li et al.	49.80
Haramura & Katto	24.48
Yagov	37.00

Fig. 9. Performance of selected prior CHF correlations as compared to measured cryogenic pool boiling CHF data from present study.

$$q''_{CHF} = \left[0.05\left(\frac{P}{P_c}\right)^{0.2} - 0.104\left(\frac{P}{P_c}\right)^{12} + 0.12\right] \times \left[1 - 0.004\left(\frac{P}{P_c}\right)\theta\right]\left|cos\left(\left(\frac{88}{180}\right)\theta\right)\right|^{0.364} \times \left[1 + 0.16\left(\frac{c_{p,f}\Delta T_{sub}}{h_{fg}}\right)\right] \times \left[\rho_g h_{fg}\left(\frac{\sigma g(\rho_f - \rho_g)}{\rho_g^2}\right)^{1/4}\right]\left[\frac{a}{g}\right]^{0.17} \times \left[e^{-1.7\left(\frac{L_c}{3\lambda_d}\right)-0.4} + 1\right]\left[0.49\left(\frac{k_w}{k_f}\right)^{0.065}\right]. \quad (8)$$

where P, P_c, ΔT_{sub}, and a are the system pressure, critical pressure, liquid subcooling, and reduced gravity, respectively, and θ is the heated surface angle with respect to gravity (0° for horizontal upward facing). Since the new correlation is modified from that of Patel et al., the ΔT_{sub}, θ, and a/g terms incorporated in the prior correlation are retained in this final correlation so as to maintain consistence in cryogenic universality. The numerical constants in Eq. (8) were determined via a nonlinear regression scheme designed to minimize predictive error. This fitting process prioritized alignment with the extensive historical experimental database, including data from the present study, in order to preserve previously captured trends while incorporating new physical insights. As a result, the revised correlation offers substantially improved agreement with experimental observations of CHF. A parity plot comparing the new correlation with the present experimental LN_2 data is shown in Fig. 10. The improved performance is quantitatively reflected by a reduced MAE of 8.31%, demonstrating a significant enhancement over prior correlations.

The new correlation captures novel physical phenomena not addressed by other predictive tools developed for cryogenic fluids. Parametric trends of the correlation with respect to characteristic length and system pressure are illustrated in Figs. 11(a) and 11(b), respectively. As the characteristic length increases, the exponential decay term causes the predicted CHF to decrease sharply at first, and eventually approach an asymptotic value regardless of L_c. Notably, at $L_c = 3\lambda_d$, the predicted CHF is within 10% of the asymptotic value for infinitely large surfaces, demonstrating the effectiveness of using $3\lambda_d$ as a threshold for distinguishing between small and effectively infinite surfaces. The influence of surface material can also be seen to be captured in the normalized thermal conductivity term, with materials possessing lower k values showing a reduced CHF. Interestingly, λ_d, which depends on fluid properties, decreases with increasing pressure. This causes surfaces that fall short of the infinite-surface criterion at ambient pressure to meet the same criterion at elevated pressures. This trend is evident in Fig. 11(b), where, for all three materials, CHF predictions for shorter heaters ($L_c = 19$ and 35 mm) converge at higher pressures with those for the $L_c = 101.1$ mm surfaces tested in this study.

The new correlation was also evaluated for its predictive capability across the entire cryogenic CHF database. This database encompasses pool boiling CHF data for various cryogens, including liquid nitrogen (LN_2), liquid helium (LHe), liquid hydrogen (LH_2), liquid oxygen (LO_2), liquid argon (LAr), and liquid methane (LCH_4). The dataset spans a range of surface orientations and includes both saturated and subcooled conditions. Parametric analyses for variances in subcooling, orientation, and gravity level can be found in Patel et al. [15]. Only metallic boiling surfaces, specifically copper, aluminum, stainless steel, gold, nickel, platinum, and Manganin, are considered, excluding ceramic materials and exotic alloys due to the difficulty in accurately determining their thermal conductivity. Microgravity data are not included in the analysis. The characteristic length is defined as the minimum continuous

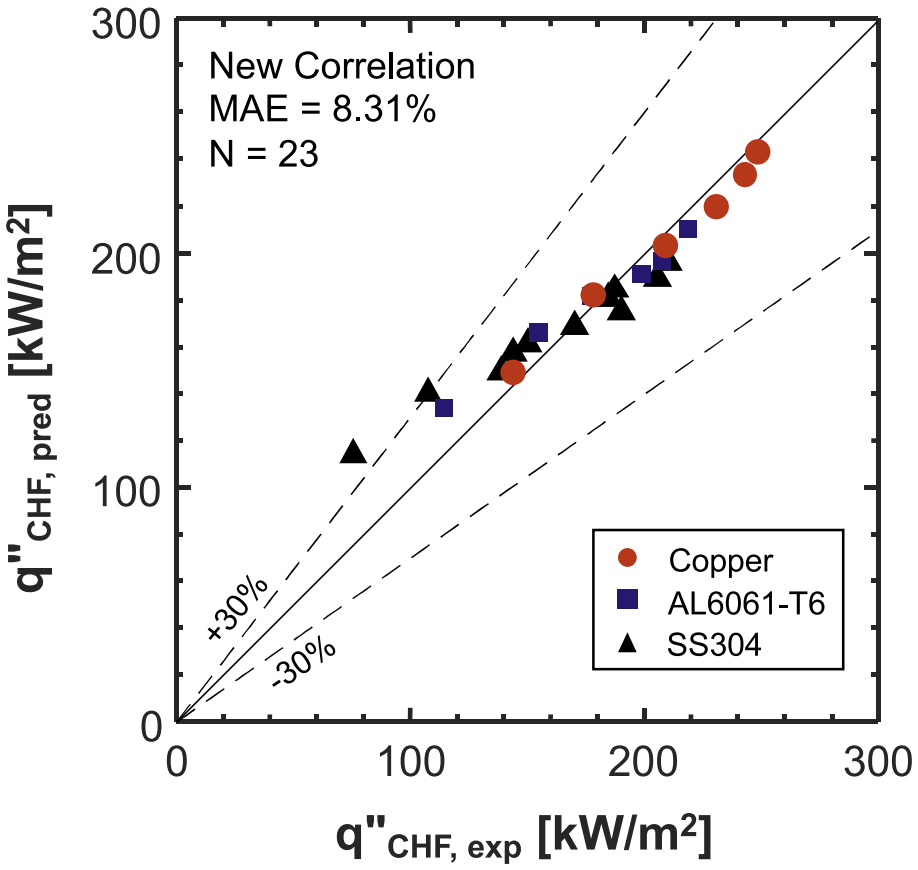

Fig. 10. Performance of new correlation for cryogenic pool boiling CHF against present LN_2 experimental data.

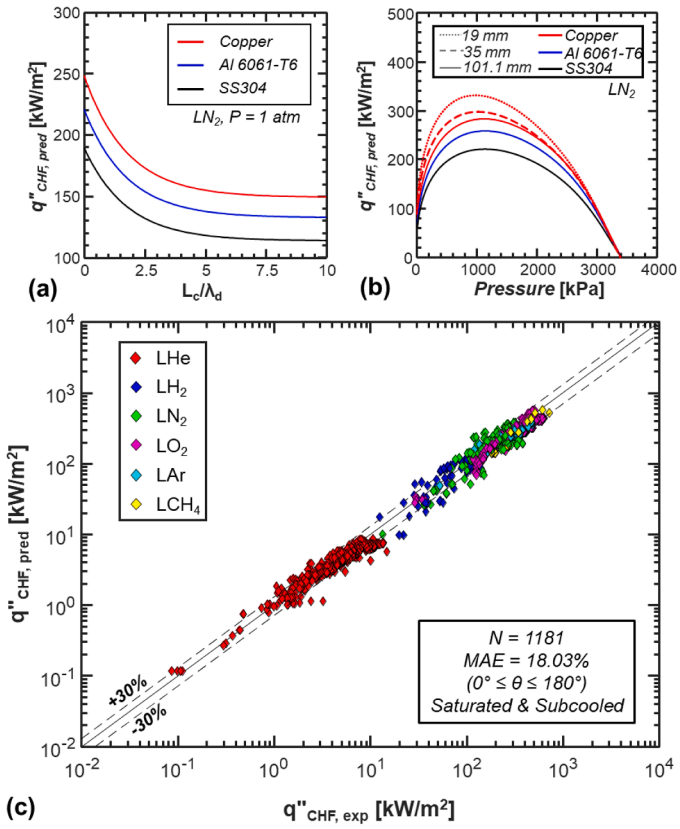

Fig. 11. Performance of new cryogenic pool boiling CHF correlation: (a) predictions for LN_2 versus dimensionless characteristic length, (b) predictions for LN_2 versus pressure, and (c) predictions entire against entire cryogenic database.

dimension of the boiling surface.

Fig. 11(c) demonstrates the high predictive accuracy of the new correlation when applied to the available CHF database, which comprises 1,181 data points. The correlation yields a MAE of 18.03%, showing consistent performance across all cryogens. MAE values for individual fluids are listed in Table 2. It is important to note that most fluids in the database lack data corresponding to asymptotically large surface sizes. While the new correlation accurately predicts the available data, further experimental investigation of large surfaces for additional fluids is necessary. The development of a universal correlation that reliably captures the CHF behavior of cryogenic fluids under a wide range of operating conditions, surface sizes, and materials is a critical asset for the design of Cryogenic Fluid Management (CFM) technologies. The trends revealed in this study, both experimentally and through the new correlation, highlight fundamental boiling phenomena that remain underrepresented in the current CHF database.

Table 2
MAE values for Eq. (8) corresponding to individual cryogenic fluids in the historical database.

Fluid	MAE [%]
LHe	17.82
LH_2	18.92
LN_2	19.12
LO_2	16.12
LAr	16.46
LCH_4	16.72

5. Conclusions

This study presented experimental measurements of saturated pool boiling CHF for LN_2 from flat, horizontal heated surfaces. The primary motivation was to investigate the influence of factors often neglected in previous studies, specifically, the effects of surface size and surface material. By properly accounting for these effects, a new CHF correlation was developed that demonstrates strong predictive accuracy across various cryogens and under both saturated and subcooled boiling conditions. Key findings are as follows:

(1) The experimental portion of the study produced CHF measurements over a wide range of pressures for three different heated surface materials: OFHC copper, aluminum 6061-T6, and 304 stainless steel. The heated surface area was deliberately chosen to approximate the behavior of an infinitely large surface, based on a size criterion that is frequently overlooked in favor of smaller surfaces in many previous investigations.
(2) The present data indicate that small heated surfaces yield comparatively higher CHF values, with CHF decreasing as the characteristic length increases, until stabilizing at an asymptotic value beyond approximately $3\lambda_d$. Surface sizes exceeding this threshold fall within the 'infinite surface' regime for which mechanistic CHF models are typically developed. Since the historical cryogenic CHF database is dominated by data for short heaters, the recent correlation proposed by Patel et al. [15], which is based on the historic database, is shown to significantly overpredict CHF for the larger surfaces used in this study.
(3) The experimental data revealed significant differences in CHF among the three heated surface materials under identical operating conditions. At atmospheric pressure, the aluminum and stainless-steel surfaces exhibited CHF reductions of 83% and 52%, respectively, compared to the OFHC copper surface, the most thermally conductive of the three. These reductions highlight the critical role of heated surface thermal conductivity in influencing CHF performance.
(4) Visualization of the interfacial dynamics during the temperature excursion at CHF offers mechanistic insight into the dependence of CHF on surface size. The transition to film boiling was observed to initiate at the center of the heated surface and propagate outward toward the periphery. The outer regions, benefiting from improved liquid access and enhanced cooling, experience delayed dryout relative to the center. This effect is particularly pronounced for smaller surfaces, which exhibit a higher circumference-to-area ratio and thus more effective edge cooling and higher CHF.
(5) Seminal CHF correlations, largely derived from data collected using small heated surfaces, were found to significantly overpredict CHF values for the large heaters used in this study. Building upon the functional form of the recent Patel et al. correlation, a new correlation is proposed that explicitly accounts for both surface size and material effects. This correlation achieves a MAE of 18.03% and demonstrates strong predictive capability across a wide range of conditions, including various cryogens (LN_2, LHe, LH_2, LO_2, LAr, and LCH_4), different metallic surface materials, both small and large characteristic lengths, saturated and subcooled boiling, various surface orientations, and a broad pressure spectrum.

CRediT authorship contribution statement

Dylan Foster: Writing – review & editing, Writing – original draft, Visualization, Validation, Software, Methodology, Investigation, Formal analysis, Data curation, Conceptualization. **Steven Darges:** Writing – review & editing, Writing – original draft, Visualization, Validation, Data curation, Conceptualization. **Nishad Damle:** Writing – original

draft, Visualization, Data curation, Conceptualization. **Sunjae Kim:** Writing – original draft, Validation, Methodology, Investigation, Formal analysis, Data curation, Conceptualization. **Issam Mudawar:** Writing – review & editing, Writing – original draft, Visualization, Validation, Supervision, Resources, Project administration, Methodology, Investigation, Funding acquisition, Formal analysis, Conceptualization. **Jason Hartwig:** Writing – original draft, Visualization, Validation, Supervision, Resources, Project administration, Investigation, Funding acquisition, Formal analysis, Conceptualization.

Declaration of competing interest

The authors declare the following financial interests/personal relationships which may be considered as potential competing interests: Issam Mudawar reports financial support was provided by NASA. Jason Hartwig reports a relationship with NASA that includes: employment. If there are other authors, they declare that they have no known competing financial interests or personal relationships that could have appeared to influence the work reported in this paper.

Acknowledgement

The authors are grateful for financial support of the National Aeronautics and Space Administration (NASA) Small Business Technology Transfer (STTR) program under a subcontract from MTS Inc. Phase II contract 80NSSC23CA009.

Appendix A

A.1. Critical heat flux for small heated surfaces

Tamvada et al. [31] proposed a CHF model based on the evaporation momentum of the boiling fluid. This model demonstrated strong agreement with experimental data across various fluids and surfaces characterized by a length scale smaller than the capillary length. The mathematical form of the model is provided in Eq. (4). In addition, they presented experimental results indicating a smooth transition between the upper CHF limit, governed by evaporation momentum, and the lower limit described by Zuber's model for an infinitely large flat surface.

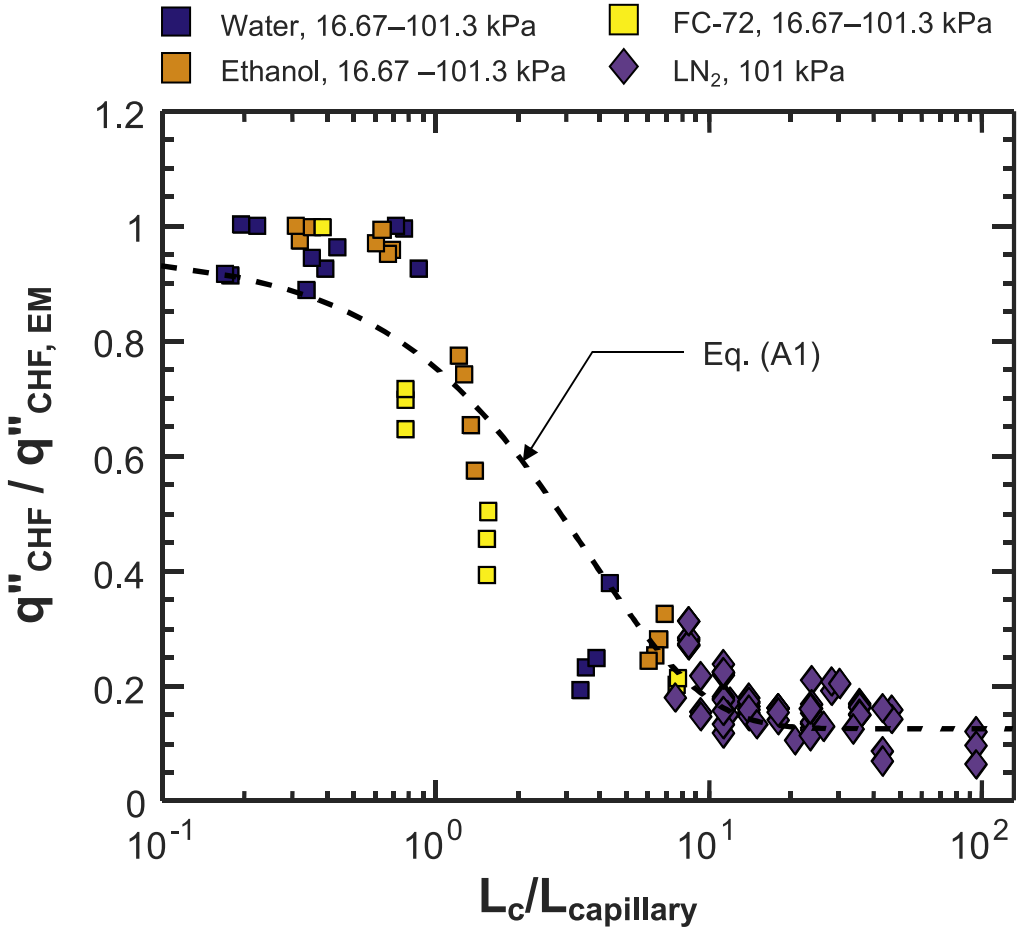

Fig. A1. Dimensionless representation of measured q''_{CHF} for saturated boiling normalized by $q''_{CHF,EM}$ predicted by the Tamvada et al. [31] model (Eq. (4)) versus the heated surface characteristic length normalized by the capillary length. Data shown are for water, FC-72, and ethanol from Tamvada et al., and LN_2 from both the current study and the historical database.

With regard to cryogenic fluids, no studies known to the present authors satisfy the criterion for CHF resulting from evaporation momentum. However, as illustrated in Fig. A1, a compilation of both current and historical experimental CHF data for saturated LN_2 from a horizontal surface at atmospheric pressure appears to follow a similar trend. This trend is also observed for room-temperature fluids when q''_{CHF} is normalized by $q''_{CHF,EM}$, the value predicted by Tamvada et al. in accordance with Eq. (4). These observations suggest that CHF for cryogenic fluids may also be bounded above by the evaporation momentum limit. Interestingly, the new correlation (Eq. (8)) can be readily adapted to capture this trend for LN_2 by refitting only

the characteristic length term to the dimensionless ratio suggested by Tamvada et al., albeit with a slightly increased MAE.

$$
\begin{aligned}
q''_{CHF} = & \left[0.05\left(\frac{P}{P_c}\right)^{0.2} - 0.104\left(\frac{P}{P_c}\right)^{12} + 0.12\right] \\
& \times \left[1 - 0.004\left(\frac{P}{P_c}\right)\theta\right]\left|cos\left(\left(\frac{88}{180}\right)\theta\right)\right|^{0.364} \\
& \times \left[1 + 0.16\left(\frac{c_{p,f}\Delta T_{sub}}{h_{fg}}\right)\right] \\
& \times \left[\rho_g h_{fg}\left(\frac{\sigma g(\rho_f - \rho_g)}{\rho_g^2}\right)^{1/4}\right]\left[\frac{a}{g}\right]^{0.17} \\
& \times \left[e^{-9\left(\frac{L_c}{3\lambda_d}\right)+1.9} + 1\right]\left[0.49\left(\frac{k_w}{k_f}\right)^{0.065}\right].
\end{aligned}
\tag{A1}
$$

Looking ahead, it is recommended that new experimental investigations be conducted to better elucidate the influence of evaporation momentum on cryogenic CHF for small surfaces.

Data availability

The data that has been used is confidential.

References

[1] NASA space technology mission directorate, civil space shortfall rankings, NASA Report, July 23rd, 2024.
[2] H.C. Hansen, W.L. Johnson, M. Meyer, A. Werkheiser, J.R. Stephens, Cryogenic Fluid Management Technologies Enabling for the Artemis Program and Beyond, AIAA, 2020, p. 4000. -.
[3] F. Chandler, D. Bienhoff, J. Cronick, G. Grayson, Propellant depots for earth orbit and lunar exploration, in: AIAA Space Conference and Exposition, Long Beach, California, AIAA SPACE, 2007, p. 6081. -.
[4] M. Kassemi, S. Hylton, O. Kartuzova, 1G and microgravity tank self-pressurization: experiments and CFD model validations across Ra and Bo regimes, Int. J. Microgravity Sci. Appl. 37 (2020) 370103.
[5] A. Majumdar, A. LeClair, J. Hartwig, Numerical Simulation of No Vent Chill and Fill of a Large Liquid Hydrogen Tank, AIAA SciTech Forum and Exposition, Orlando, Florida, 2024.
[6] J. Hartwig, J. Vera, Numerical modeling of the transient chilldown process of a cryogenic propellant transfer line, in: AIAA Aerospace Sciences Meeting, Kissimmee, Florida, AIAA, 2015, p. 0473. -.
[7] J. Hartwig, J. Stephens, N. Rhys, J. Clar, A. LeClair, A. Majumdar, Test data analysis of the thermodynamic vent system-augmented top spray injector liquid nitrogen transfer experiments, Int. J. Heat Mass Transf. 194 (2022) 122986.
[8] S. Kim, D. Foster, N. Damle, I. Mudawar, J. Hartwig, Experimental investigation of flow orientation effects on cryogenic flow boiling, Int. J. Heat Mass Transf. 220 (2024) 124940.
[9] S. Kim, N. Damle, D. Foster, S. Darges, J. Hartwig, I. Mudawar, Critical heat flux of cryogenic flow boiling under terrestrial, partial, and reduced gravity conditions, Int. J. Heat Mass Transf. 245 (2025) 126957.
[10] J.N. Chung, J. Dong, H. Wang, B.H. Huang, J. Hartwig, Demonstration of charge-hold-vent (CHV) and no-vent-fill (NVF) in a simulated propellent storage tank during tank-to-tank cryogen transfer in microgravity, Microgravity 10 (2024) 1–12.
[11] I. Mudawar, S.J. Darges, V.S. Devahdhanush, Critical heat flux for flow boiling with saturated two-phase inlet in microgravity onboard the international space station, Int. J. Heat Mass Transf. 233 (2024) 126017.
[12] I. Mudawar, V.S. Devahdhanush, S.J. Darges, M.M. Hasan, H.K. Nahra, R. Balasubramaniam, J.R. Mackey, Heat transfer and interfacial flow physics of microgravity flow boiling in single-side-heated rectangular channel with subcooled inlet conditions – experiments onboard the international space station, Int. J. Heat Mass Transf. 207 (2023) 123998.
[13] I. Mudawar, S.J. Darges, V.S. Devahdhanush, M.M. Hasan, H.K. Nahra, R. Balasubramaniam, J.R. Mackey, Two-phase flow instabilities during microgravity flow boiling onboard the international space station, Int. J. Heat Mass Transf. 234 (2024) 126102.
[14] J.W. Hartwig, A. Asensio, S.R. Darr, Assessment of existing two phase heat transfer coefficient and critical heat flux on cryogenic flow boiling quenching experiments, Int. J. Heat Mass Transf. 93 (2016) 441–463.
[15] R. Patel, M. Meyer, J. Hartwig, I. Mudawar, Review of cryogenic pool boiling critical heat flux databases, assessment of models and correlations, and development of new universal Correlations, Int. J. Heat Mass Transf. 190 (2022) 122579.
[16] R.J. Grotenrath, R. Balasubramaniam, J.W. Smith, P.A. Giddens, W.L. Johnson, Comparison of liquefaction testing with liquid nitrogen and liquid oxygen, in: Cryogenic Engineering Conference, Honolulu, HI, 2023.
[17] G. Liang, I. Mudawar, Pool boiling critical heat flux (CHF) – part 2: assessment of models and correlations, Int. J. Heat Mass Transf. 117 (2018) 1368–1383.
[18] I. Mudawar, T.A. Deiters, A universal approach to predicting temperature response of metallic parts to spray quenching, Int. J. Heat Mass Transf. 37 (1994) 347–362.
[19] I. Mudawar, R.A. Houpt, Mass and momentum transport in smooth falling liquid films laminarized at relatively high Reynolds numbers, Int. J. Heat Mass Transf. 36 (1993) 3437–3448.
[20] C.R. Kharangate, H. Lee, I. Mudawar, Computational modeling of turbulent evaporating falling films, Int. J. Heat Mass Transf. 81 (2015) 52–62.
[21] M.T. Meyer, I. Mudawar, C.E. Boyack, C.A. Hale, Single and two-phase cooling with an array of rectangular jets, Int. J. Heat Mass Transf. 49 (2006) 17–29.
[22] T.C. Willingham, I. Mudawar, Channel height effects on forced-convection boiling and critical heat flux from a linear array of discrete heat sources, Int. J. Heat Mass Transf. 35 (1992) 1865–1880.
[23] C.O. Gersey, I. Mudawar, Effects of heater length and orientation on the trigger mechanism for near-saturated flow boiling critical heat flux - II. Critical heat flux model, Int. J. Heat Mass Transf. 38 (1995) 643–654.
[24] T.J. LaClair, I. Mudawar, Thermal transients in a capillary evaporator prior to the initiation of boiling, Int. J. Heat Mass Transf. 43 (2000) 3937–3952.
[25] H. Lee, I. Park, I. Mudawar, M.M. Hasan, Micro-channel evaporator for space applications-1. Experimental pressure drop and heat transfer results for different orientations in earth gravity, Int. J. Heat Mass Transf. 77 (2014) 1213–1230.
[26] M.K. Sung, I. Mudawar, Single-phase and two-phase heat transfer characteristics of low temperature hybrid micro-channel/micro-jet impingement cooling module, Int. J. Heat Mass Transf. 51 (2008) 3882–3895.
[27] M.K. Sung, I. Mudawar, Single-phase and two-phase hybrid cooling scheme for high-heat-flux thermal management of defense electronics, J. Electron. Packag. 131 (2009) 021013.
[28] N. Zuber, Hydrodynamic aspects of boiling heat transfer, AEC Report No. AECU-4439, United States Atomic Energy Commission, Oak Ridge, Tennessee, 1959.
[29] J.H. Lienhard, V.K. Dhir, Hydrodynamic prediction of peak pool-boiling heat fluxes from finite bodies, J. Heat Transf. 95 (1973) 152–158.
[30] J.H. Lienhard, V.K. Dhir, D.M. Riherd, Peak pool boiling heat-flux measurements on finite horizontal flat plates, J. Heat Transf. 95 (1973) 477–482.
[31] S. Tamvada, D. Attinger, S. Moghaddam, On critical heat flux and its evaporation momentum and hydrodynamic limits, Int. J. Heat Mass Transf. 203 (2023) 123837.
[32] A. Steinchen, K. Sefiane, Stability analysis of the pool-boiling crisis, J. Phys. Condens. Matter 8 (1996) 9565–9568.
[33] F. Tachibana, M. Akiyama, H. Kawamura, Non-hydrodynamic aspects of pool boiling burnout, J. Nucl. Sci. Technol. 4 (1967) 121–130.
[34] Y. Mei, Y. Shao, S. Gong, Y. Zhu, H. Gu, Effects of surface orientation and heater material on heat transfer coefficient and critical heat flux of nucleate boiling, Int. J. Heat Mass Transf. 121 (2018) 632–640.
[35] V. Grigoriev, V. Klimenko, Y. Pavlov, Y. Ametistov, The influence of some heating surface properties on the critical heat flux in cryogenic liquids boiling, in: Proc. Int. Heat Transf Conf Digital Library, Begel House Inc., 1978.
[36] C. Bombardieri, C. Manfletti, Influence of wall material on nucleate pool boiling of liquid nitrogen, Int. J. Heat Mass Transf. 94 (2016) 1–8.
[37] A. Bar-Cohen, A. McNeil, Parametric effects on pool boiling critical heat flux in highly wetting liquids, in: Proc. Engineering Foundation Conf. on Pool and External Flow Boiling, Santa Barbara, CA, 1992, pp. 171–176.
[38] K. Stephan, M. Abdelsalam, Heat transfer correlations for natural convection boiling, Int. J. Heat Mass Transf. 23 (1980) 73–87.
[39] P. Kosky, Studies in Boiling Heat Transfer to Cryogenic Liquids, Ph.D. thesis, University of California, Berkeley, 1966.
[40] F. Chavagnat, High-resolution experimental measurements and mechanistic modelling of saturated cryogenic pool boiling heat transfer, Ph.D. thesis, Massachusetts Institute of Technology, 2024.
[41] X. Zhang, J. Chen, W. Xiong, T. Jin, Visualization study of nucleate pool boiling of liquid nitrogen with quasi-steady heat input, Cryogenics 72 (2015) 14–21.

[42] A.N. Pavlenko, D.V. Kuznetsov, V.P. Bessmeltsev, Experimental study on heat transfer and critical heat flux during pool boiling of nitrogen on 3D printed structured copper capillary-porous coatings, J. Eng. Thermophys. 30 (2021) 341–349.
[43] L. Bewilogua, R. Knöner, H. Vinzelberg, Heat transfer in cryogenic liquids under pressure, Cryogenics 15 (1975) 121–125.
[44] M. Mann, K. Stephan, P. Stephan, Influence of heat conduction in the wall on nucleate boiling heat transfer, Int. J. Heat Mass Transf. 43 (2000) 2193–2203.
[45] J. Li, L.E. O'Neill, M.G. Izenson, C.R. Kharangate, Data consolidation, correlations assessment, and new correlation development for pool boiling critical heat flux specific to cryogenic fluids, Int. J. Heat Mass Transf. 213 (2023) 124315.
[46] Y. Haramura, Y. Katto, A new hydrodynamic model of critical heat flux, applicable widely to both pool and forced convection boiling on submerged bodies in saturated liquids, Int. J. Heat Mass Transf. 26 (1983) 389–399.
[47] V.V. Yagov, Is a crisis in pool boiling actually a hydrodynamic phenomenon? Int. J. Heat Mass Transf. 73 (2014) 265–273.